

# Selective trapping and concentration of nanoparticles and viruses in dual-height nanofluidic channels†

Mark N. Hamblin,<sup>a</sup> Jie Xuan,<sup>b</sup> Daniel Maynes,<sup>c</sup> H. Dennis Tolley,<sup>d</sup> David M. Belnap,<sup>b</sup> Adam T. Woolley,<sup>b</sup> Milton L. Lee<sup>b</sup> and Aaron R. Hawkins<sup>\*a</sup>

Received 14th August 2009, Accepted 19th October 2009

First published as an Advance Article on the web 18th November 2009

DOI: 10.1039/b916746c

Nanofluidic systems offer advantages for chemical analysis, including small sample volumes, size-selective particle trapping, sample concentration and the ability to separate and detect single molecules. Such systems can be fabricated using planar nanochannels, which rely on standard photolithographic techniques. Nanochannel fluid flow can be driven by capillary action, which benefits from simple injection and reasonably high flow rates. We demonstrate an analysis chip fabricated with planar nanochannels that consist of two adjoining segments of different heights. When nano-analytes elute through the channel, they become physically trapped when the channel dimensions shrink below the size of the particles. We demonstrate the capability of these devices to trap and concentrate by using the following: 120-nm polymer beads, 30-nm polymer beads, *Herpes simplex* virus 1 capsids, and hepatitis B virus capsids. Each species was fluorescently labeled and its resulting fluorescent signal was detected using a cooled CCD camera. We show how the signal-to-noise ratio of trapped analyte intensity varies linearly with analyte concentration. The goal of this work is to eventually perform size-based fractionation of a variety of nanoparticles, including biomolecules such as proteins.

## 1 Introduction

Channels or capillaries that possess at least one dimension in the range from 1 nm to 100 nm through which fluids are passed can be classified as nanofluidic devices. Nanofluidics offer a number of advantages in chemical analysis, yet simultaneously suffer from complications due to their small dimensions.<sup>1</sup> Several of these advantages include the use of minute sample volumes, the ability to separate and detect single particles, and the ability to employ channel dimensions in fractionation.<sup>2</sup> Alternatively, challenges include developing fabrication methods that are reproducible, robust, and fast. Furthermore, as channel dimensions shrink, several well-founded fluid flow techniques become ineffective. For example, overlapping electric double layers adversely decrease electroosmotic pumping.<sup>3</sup> Pressurized pumping is also inefficient because nanofluidic channels generate high hydraulic resistances.<sup>3</sup> To overcome these weaknesses, researchers must pursue innovative fabrication, fluid flow and separation techniques.

Nanochannel cross-sectional profiles can be divided into two main categories, *i.e.*, non-planar and planar. Non-planar methods produce nanochannels with dimensions that are

approximately on the same scale, while planar nanochannels typically have one cross-sectional dimension that is many times larger than the other dimension. For non-planar profiles, lithographic techniques define the nanometre dimensions of the channels. Lithographic dimensions in the nanometre range are possible using techniques such as extreme ultraviolet (EUV) lithography, X-ray lithography, and electron beam lithography (EBL). However, each of these systems suffers drawbacks, including high tooling costs and slow operation.<sup>4,5</sup> In contrast, planar nanochannels rely on standard thin film processes which are inexpensive, fast, and can control the channel height to within several nanometres.

The two most popular methods for fabricating planar nanochannels are bonding and sacrificial etching. In bonding, a substrate with etched channels adheres thermally, electrically or chemically to a flat cover-plate. Bonded nanofluidic channels are reported with heights between 20 nm and 900 nm.<sup>6–9</sup> Despite advances in bonding techniques, etched nanochannels with high aspect ratios can collapse during enclosure and come into contact with the cover plate. This effect can be avoided using sacrificial etching, which employs a patterned thin film to define the sacrificial channel core.<sup>10</sup> Once the core is encapsulated by a structural thin film, it is removed by a chemical etchant to result in a hollow, planar nanochannel.

Sacrificial cores have been made from various thin film materials including amorphous silicon, polysilicon, polymers, and metals. Using amorphous silicon, Stern *et al.*<sup>11</sup> fabricated a 20-nm tall channel. Other researchers have fabricated nanochannels based on polysilicon cores that range in height from 5 nm to 270 nm.<sup>12–15</sup> Polymer cores have been used to produce microfluidic channels<sup>16–20</sup> as well as nanofluidic channels as shallow as 100 nm.<sup>21</sup> Thin film metals comprise another set of

<sup>a</sup>Department of Electrical and Computer Engineering, Brigham Young University, Provo, UT, 84602, USA. E-mail: aaronrhawkins@gmail.com; Fax: +1 801-422-0201; Tel: +1 801-422-8693

<sup>b</sup>Department of Chemistry and Biochemistry, Brigham Young University, Provo, UT, 84602, USA

<sup>c</sup>Department of Mechanical Engineering, Brigham Young University, Provo, UT, 84602, USA

<sup>d</sup>Department of Statistics, Brigham Young University, Provo, UT, 84602, USA

† Electronic supplementary information (ESI) available: Video showing nano-analyte flow in the channels. See DOI: 10.1039/b916746c

sacrificial materials that can be deposited as thin as a few nanometres, and benefit from rapid etching.<sup>22–24</sup>

Most nanofluidic separations rely on electrophoresis, porous membranes, networks of micro-pillars, or variable-height nanofluidic channels.<sup>25</sup> Electrophoretic separations have been demonstrated in capillaries ranging in diameter from 770 nm to 270 nm.<sup>13,26</sup> However, when the electric double layer is on the order of the characteristic dimensions of a nanofluidic channel, the flow profile becomes highly nonuniform and the nature of the separation deviates from classical electrophoresis.<sup>27,28</sup> Another separation medium, membranes, have been fabricated with pores ranging in diameter from 260 nm to 5 nm,<sup>29–31</sup> but can easily break when pressurized. Arrays of micro-pillars<sup>8,12</sup> and variable-height nanofluidic channels<sup>7,32</sup> have been shown to successfully sieve and separate DNA. However, these separation methods are limited to entropic trapping and reptation, which limits the scope of the separation to analytes which can easily deform.

A promising alternative nanofluidic separation mechanism is size-specific trapping. Trapping systems can be driven by capillary action, which has been well-characterized for small capillaries,<sup>33</sup> and has been shown to be an effective filling force for planar nanochannels.<sup>34–36</sup> Capillary filling is limited to the time required to initially fill a channel, and additional fluid flow can be achieved through evaporation at the channel end.<sup>37,38</sup> A size-specific trapping nanofluidic device filled *via* capillary action was demonstrated by Wang *et al.*,<sup>39,40</sup> where gold nanoparticles became trapped while eluting from a micro-channel to a nanochannel that was smaller than the gold particles. Analytes adsorbed to the trapped gold particles were detected using surface-enhanced Raman spectroscopy (SERS). This method relied on the ability and extent to which analytes adsorbed to the gold particles. An extension of this approach that negates the need for adsorbed analytes utilizes the micro-fluidic/nanofluidic junction for directly trapping and concentrating analytes.

We present a nanofluidic, size-specific trapping device that is fast-filling, robust, fabricated using standard silicon manufacturing processes and capable of separating and concentrating nanoparticles based on their size. Separation is achieved using a two-segment nanochannel, as shown in Fig. 1. The first channel segment is tall enough to allow the analyte to enter, but the second segment is sufficiently shallow to trap the analyte, as shown in Fig. 1(b). Two different devices are utilized in this paper, consisting of tall and short segments of 190 nm and 65 nm for one device and 145 nm and 25 nm for the other. This allows separation and concentration based on analyte size and shape. Trapped analytes are detected by their fluorescent signal upon LED excitation. Analytes flow and are trapped under the influence of capillary action. The use of capillary action as the filling mechanism offers the advantage of reasonable flow rates and simple injection. Systems that rely on pressurized injection suffer from the complexity of moving parts, while systems that rely on electrokinetic flow require electrolyte-compatible electrodes and high voltages. We outline the fabrication steps, sample preparation, and detection system, and demonstrate size-selective trapping and detection of 120-nm polymer beads, 30-nm polymer beads, *Herpes simplex* virus 1 (HSV-1) capsids, and hepatitis B virus (HBV) capsids.

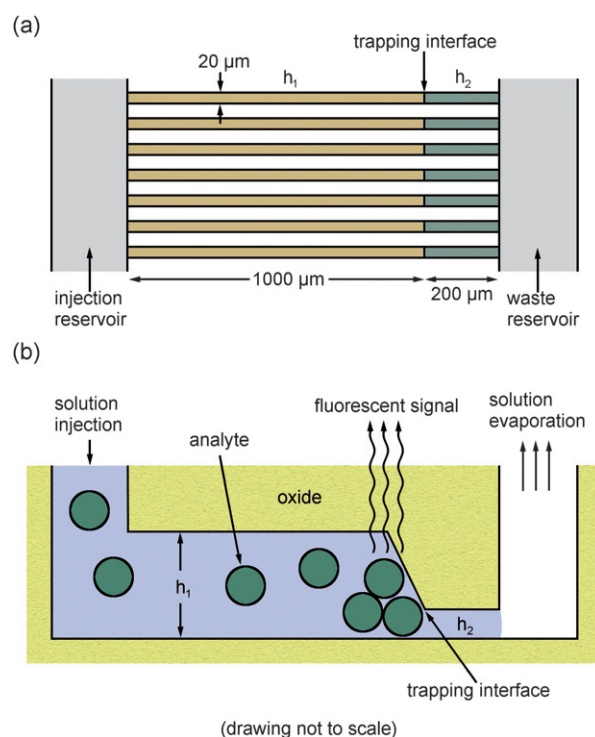


**Fig. 1** Illustration showing the operation of the trapping device. (a) Each chip consists of 200 parallel 20- $\mu\text{m}$ -wide channels. The taller segment,  $h_1$ , is 1000  $\mu\text{m}$  long while the shorter segment,  $h_2$ , is 200  $\mu\text{m}$  long. Solution is introduced through the injection reservoir and collected at the waste reservoir. (b) The solution initially flows *via* capillary action, and once the channels fill, subsequent flow is limited by evaporation at the waste reservoir. Analytes that are too small to pass into the second, shorter channel segment become trapped at the interface. The trapped analytes are then detected by recording their visible fluorescent signal with a CCD camera.

## 2 Experimental

### 2.1 Fabrication

This paper describes two sets of nanofluidic devices fabricated with sacrificial cores. The first set contained channels transitioning from 190 nm to 65 nm and the second set contained channels transitioning from 145 nm to 25 nm. Each of the taller segments was 1000  $\mu\text{m}$  long and each of the shorter segments was 200  $\mu\text{m}$  long. Each device contained 200 nanochannels in parallel. Fig. 2(a–i) illustrates the fabrication process, and Fig. 2(j) shows a completed chip next to a U.S. quarter to illustrate chip dimensions. The process begins with (a) coating a substrate with a layer of approximately 200 nm of plasma-enhanced chemical vapor deposited (PECVD) silicon dioxide, which will form a wettable surface for the bottom of the channel. A layer of sacrificial aluminium is then deposited to form the short channel segment, which is 65 nm or 25 nm, depending on the device. (b) AZ nLOF 2020 photoresist is spun-on and patterned to define an area where another sacrificial layer will be deposited. (c) A second sacrificial layer of aluminium is deposited to form the tall channel segment. This layer, combined with the previous one, is 190 nm or 145 nm, depending on the device. (d) The photoresist is lifted-off using *N*-methylpyrrolidone (NMP)

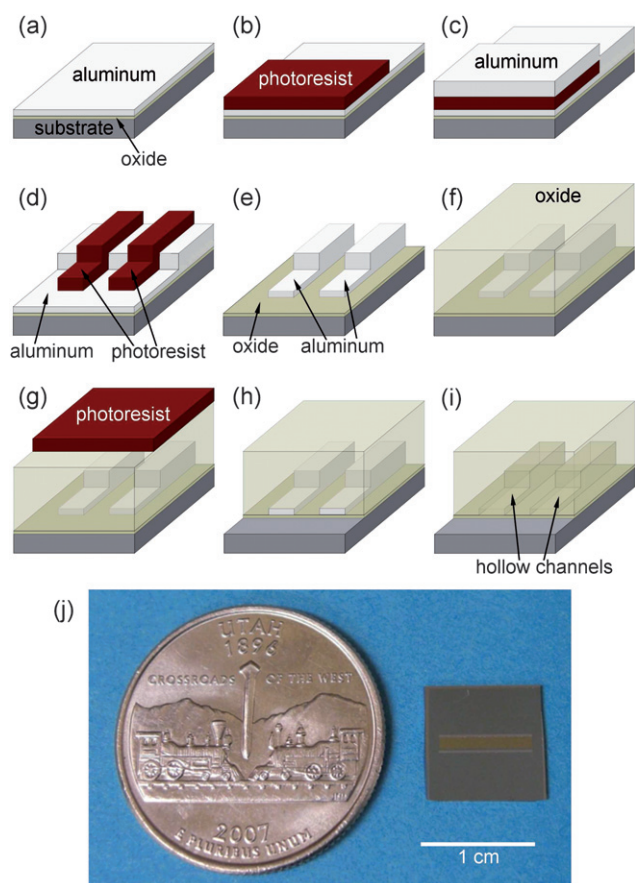


**Fig. 2** Fabrication steps involved in making two-segment sacrificial nanochannels. (a) A silicon or glass substrate is coated with a layer of 200 nm of PECVD silicon dioxide and a sacrificial layer of aluminium. (b) Photoresist is spun-on and patterned, where the unmasked area defines the tall channel segments. (c) A second layer of aluminium is deposited. (d) The photoresist is lifted off, followed by patterning channel lines in a new layer of photoresist. (e) The exposed aluminium is then etched, following which the remaining photoresist is dissolved in acetone. (f) The aluminium cores are coated with 3  $\mu\text{m}$  of PECVD silicon dioxide. (g) Photoresist is applied and patterned to define reservoirs and expose the sacrificial cores. (h) The reservoirs are etched using BOE. (i) The exposed aluminium cores are etched using aqua regia. Completed nanochannels are 20  $\mu\text{m}$  wide and 1200  $\mu\text{m}$  long. (j) Photograph of a silicon die containing a completed device set next to a U.S. quarter.

heated to 60  $^{\circ}\text{C}$ , leaving two distinct areas of varying heights of sacrificial aluminium. AZ 3330 photoresist is then spun-on and patterned to define the channels. (e) The exposed aluminium is etched using commercial etchant (Transene) heated to 50  $^{\circ}\text{C}$ , and the remaining photoresist is dissolved in acetone. (f) A capping layer of approximately 3  $\mu\text{m}$  of PECVD silicon dioxide is deposited over the cores. (g) AZ 3330 photoresist is spun-on and patterned to define reservoirs and provide access to the sacrificial cores. (h) The exposed oxide is etched using a buffered oxide etchant (BOE) composed of hydrofluoric acid, and the masking photoresist is dissolved in acetone. (i) The exposed aluminium cores are then etched using a dilute solution of aqua regia (hydrochloric acid and nitric acid) heated to 80  $^{\circ}\text{C}$ . Once the sacrificial etching process is complete, hollow nanofluidic channels consisting of two heights remain.

## 2.2 Sample preparation

**120-nm beads.** A solution of polystyrene beads with diameters of  $120.4 \pm 4.7$  nm was obtained from Polysciences, Warrington, PA, product number 18719. The beads were suspended in a mixture of 97.5% water and 2.5% benzene, and were diluted to concentrations of  $4.55 \times 10^{11}$  particles  $\text{mL}^{-1}$ ,  $4.55 \times 10^{10}$  particles  $\text{mL}^{-1}$ , and  $4.55 \times 10^9$  particles  $\text{mL}^{-1}$  using 100 mM Tris(HCl) at a pH of 8.3. The beads were optimally excited at 529 nm and had an emission maximum at 546 nm. All experimental runs utilized between 1  $\mu\text{L}$  and 5  $\mu\text{L}$  of solution injection.

**30-nm beads.** A solution of polyacrylonitrile beads with diameters of  $30 \pm 5$  nm was obtained from Sigma-Aldrich, St. Louis, MO, product number 43666. The beads were suspended in 10 mM MES in water with 15 mM sodium azide, and were diluted to concentrations of  $3.54 \times 10^{13}$  particles  $\text{mL}^{-1}$ ,  $3.54 \times 10^{12}$  particles  $\text{mL}^{-1}$ , and  $3.54 \times 10^{11}$  particles  $\text{mL}^{-1}$  using 100 mM Tris(HCl) at a pH of 8.3. The beads were optimally excited at 470 nm and had an emission maximum at 611 nm.

**HSV-1 capsids.** A suspension of *Herpes simplex* virus type 1 was obtained from the laboratory of J. Brown (see Acknowledgements). HSV-1 has an icosahedral capsid with an average diameter of approximately 125 nm.<sup>41</sup> To enable fluorescent detection, the capsids were labeled with fluorescein isothiocyanate (FITC) (Invitrogen, Eugene, OR) by diluting 100  $\mu\text{L}$  of the virus suspension with 100  $\mu\text{L}$  of a labeling solution of 100 mM bicarbonate buffer adjusted to a pH of 9.0. The virus suspension was incubated with 10  $\mu\text{L}$  of FITC stock solution ( $\sim 2$  mM in dimethyl sulfoxide obtained from Mallinckrodt Baker Inc., Paris, Kentucky) in the dark at room temperature for 24 h. To remove excess FITC and concentrate the capsids for trapping, the virus suspension was first diluted to 2 mL with 50 mM borate buffer at pH 8.3 and then centrifuged at 6000 rpm with an SS-34 rotor for 15 min using centrifugal membrane filters with a cutoff of 30 000 Da. This step was repeated to produce a final volume of 200  $\mu\text{L}$  of virus suspension. The viral protein concentration was 2.3  $\text{mg mL}^{-1}$ , as determined from DC protein assay using  $\alpha$ -1-antitrypsin as the standard, which corresponds to approximately  $5.4 \times 10^{12}$  particles  $\text{mL}^{-1}$ .

**HBV capsids.** A suspension of hepatitis B virus capsids was obtained from the laboratory of A. Zlotnick (see Acknowledgements). HBV has an icosahedral capsid approximately 30 nm in diameter.<sup>42</sup> The fluorescent labeling and preparation steps for HBV capsids were identical to those used for preparing HSV-1 capsids. The viral concentration was approximately 6.76  $\text{mg mL}^{-1}$  as determined from DC protein assay using BSA as the standard, which corresponds to approximately  $9.44 \times 10^{14}$  particles  $\text{mL}^{-1}$ .

## 2.3 Electron microscopy

Before and after the labeling process, a Philips Tecnai F30 transmission electron microscope (TEM) (FEI, Hillsboro, OR), operated at 300 kV and at a magnification of 39 000 $\times$ , captured images of the solutions. This was done to ensure that there were no other virus species in the sample, that the derivatized virus



retained its original structure, and that derivatization did not result in increased viral aggregation. TEM micrographs for HSV-1 capsids and HBV capsids are shown in Fig. 3(a) and 3(b), respectively.

## 2.4 Detection system

The microscopy detection system included an Olympus BX60M microscope (Olympus, Center Valley, PA) fitted with a Thorlabs 625 mW LED light source (product number MBLED, Thorlabs, Newton, NJ) that emitted at a center wavelength of 470 nm. A Semrock BrightLine filter cube, product number FITC-LP01-Clinical-OMF (Semrock, Rochester, NY), was used. The filter cube employed a long-pass dichroic mirror with an edge wavelength of 515 nm and an excitation filter with a center wavelength of 475 nm. The fluorescent signal was detected using a Photometrics CoolSNAP HQ cooled CCD camera (Photometrics, Tucson, AZ), and 12-bit frames were captured every 753 ms for each data set.

## 2.5 Data analysis

The net normalized signal intensity was calculated from acquired images by (1) defining a single-pixel thick line with a pre-defined width along the the brightest region of the trapped analytes, (2) calculating the mean value of pixel intensity across this line, (3) defining an area in a region adjacent to the signal that contained only background signal, (4) subtracting the mean of the background area from the mean of the signal region to create a net signal intensity, and (5) dividing each data set by its maximum value over a given range to produce a normalized intensity.

## 3 Results and discussion

Before covering particle trapping experiments, it is worth mentioning theoretical flow rates. During the initial filling phase, solution flows due to capillary action. The Washburn formula<sup>33</sup> models this flow by relating time,  $t$ , and meniscus position,  $x$ , as

$x^2 \propto t$ . From this relation it is apparent that the filling velocity decreases as the solution progresses along the length of the channel. The slowest filling speeds therefore occur at the channel end, which theory predicts to be 250 ms for channels stepping in size from 190 nm to 65 nm and 354 ms for channels stepping in size from 145 nm to 25 nm. Experimental results indicate that the flow behavior of these nanochannels very closely matches the slope provided by  $x^2 \propto t$ .

Once the channels have filled *via* capillary action, further flow is driven by evaporation of the solution at the waste reservoir. The evaporative flow rate is proportional to the ambient partial pressure of water vapor, and the partial pressure is expected to locally increase at the waste reservoir over time so that as the air becomes saturated the flow rate becomes very limited. Goedecke *et al.*<sup>37</sup> illustrated the high degree of variability in evaporative flow rates when the air surrounding the evaporative area remains stagnant. Simple experimental analysis has yielded flow rates as high as  $322 \mu\text{m s}^{-1}$ , although it is apparent that evaporative flow rates decrease with time. All filling experiments were performed at room temperature in a laboratory with an average relative humidity of 30%.

In order to test the feasibility of trapping and concentrating nano-scale species, we developed nanofluidic structures with channels that consisted of two interfacing segments of different heights. The initial tests utilized spherical, fluorescently-labeled polymer beads with average diameters of 120 nm and 30 nm. Once it was established that these particles could be trapped and detected, we analyzed fluorescently-labeled HSV-1 capsids and HBV capsids. These viruses were chosen because their average diameters of 125 nm and 30 nm closely matched the average diameters of the polymer beads. Fig. 4 demonstrates the ability

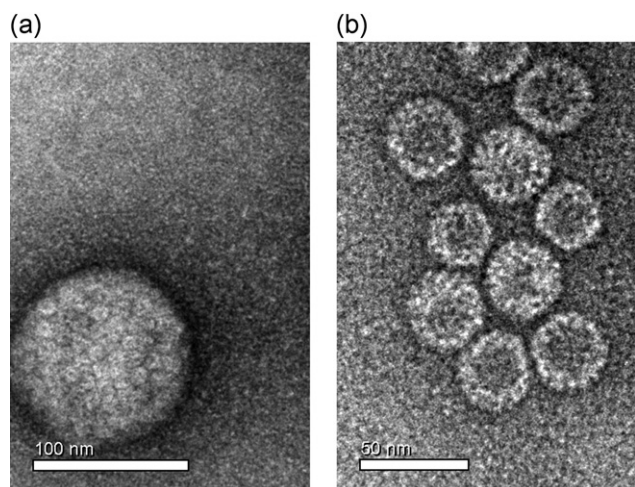


**Fig. 3** TEM micrographs showing FITC-conjugated capsids of (a) HSV-1 and (b) HBV. HSV-1 capsids have an average diameter of  $\sim 125$  nm, and HBV capsids have an average diameter of  $\sim 30$  nm. These micrographs demonstrate that the capsid structures remain intact following labeling and sample concentration.

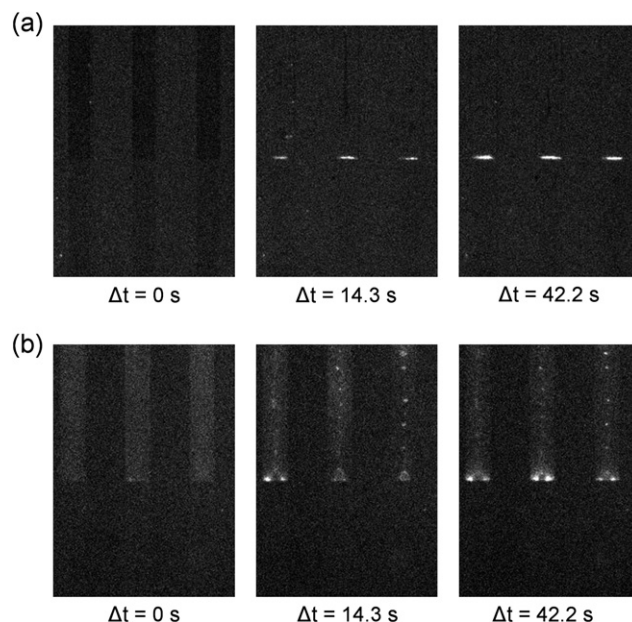


**Fig. 4** Time lapse photographs showing an increase in fluorescent signal of (a) trapped HSV-1 capsids and (b) trapped HBV capsids. Trapped analytes appear as white bands that increase in intensity over time. In (a), the channel interface steps from a height of 190 nm to 65 nm, and in (b) the channel interface steps from a height of 145 nm to 25 nm. The signal intensity increased over time until the injection reservoir dried out.

of these devices to trap HSV-1 and HBV capsids. This Figure also shows an increase in fluorescent signal intensity with time. Also discernible in this Figure is the affinity that HBV capsids exhibit near the corners of the channel interface, as evidenced by the greater signal intensity at the corners. For all experiments, the fluorescent signal was confined to the channel interface and was not detected at the waste reservoir. The electronic supplementary information accompanying this article shows HSV-1 capsids being trapped at a channel interface stepping from 190 nm to 65 nm over the course of nearly a minute.<sup>†</sup>

One way to demonstrate the capability of trapping is by analyzing how the fluorescent signal changes over time for several nanoparticles. Fig. 5 is a plot demonstrating the normalized intensity increase over time for 120-nm beads at a concentration of  $4.55 \times 10^{10}$  particles  $\text{mL}^{-1}$ , 30-nm beads at a concentration of  $3.54 \times 10^{12}$  particles  $\text{mL}^{-1}$ , HSV-1 capsids, and HBV capsids. In order to trap the 120-nm beads and the HSV-1 capsids, a device with segment heights of 190 nm and 65 nm was used. To trap the 30-nm beads and the HBV capsids, a device with segment heights of 145 nm and 25 nm was used. In the Figure,  $t = 0$  corresponds to the point at which the first fluorescent signal at the interface is detected. For all experimental runs, the channels filled completely due to capillary action before a signal was detected at the interface. For the polymer bead experiments, the intensity then increased steadily until  $t \approx 12$  s, at which point the slope of each curve decreased. The time delay between channel filling and the first detected signal may be attributed to titration of the solution by acidic silanol groups on the silicon oxide walls.<sup>43</sup> Similarly, variation in the slope of the intensity was likely due to titration. As the titrated solution flowed through the channel *via* evaporation at the channel outlet (*i.e.*, evaporative flow), the solution surrounding the trapped analytes became less acidic and the fluorescent signal intensified. This effect continued until the solution at the trapping interface reached a pH at which fluorescence was no longer suppressed (*i.e.* at  $t \approx 12$  s). The increasing signal intensity thereafter was caused by new analytes being trapped at the interface due to evaporative flow. Furthermore, in

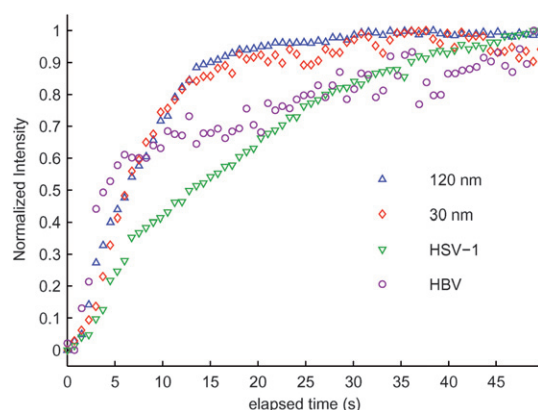


**Fig. 5** Normalized fluorescent signal intensity *versus* time for particles being trapped at the channel interface. The 120-nm beads and HSV-1 capsids were trapped in channels stepping in height from 190 nm to 65 nm, and the 30-nm beads and HBV capsids were trapped in channels stepping in height from 145 nm to 25 nm. The plotted data represent the normalized, mean intensity values for 17 to 32 data sets, depending on the particle types.

Fig. 5 the curves representing the virus capsids were more flattened than the curves representing the polymer beads. This result was likely due to some retention mechanism caused by interaction between the virus capsids and the channel walls.

Comparing the fluorescent signal for various analyte concentrations to the background noise can provide information about the ultimate sensitivity of the detection system and test the linearity between particle number and intensity. To determine the signal-to-noise ratio (SNR) of analytes trapped in a channel, it was necessary to define a standard method for each data set. The net signal was calculated as outlined previously and then divided by the standard deviation of the background lines to generate the SNR for each channel. This technique was applied to data from several channels at a pre-determined point in time, and the resulting values are plotted in Fig. 6(a–b) for several dilutions of 120-nm beads and 30-nm beads. These plots demonstrate an approximately linear increase in SNR with increasing particle concentration. Multiplying particle concentration by the volume of one channel gives the number of particles initially loaded in each channel, which provides an approximation for the number of particles trapped at each channel interface. This is shown by the top  $x$ -axis in Fig. 6(a–b). Fig. 6(c) shows a 3D plot of the normalized signal intensity of an area surrounding a channel interface for trapped 120-nm beads at a concentration of  $4.55 \times 10^{10}$  particles  $\text{mL}^{-1}$ .

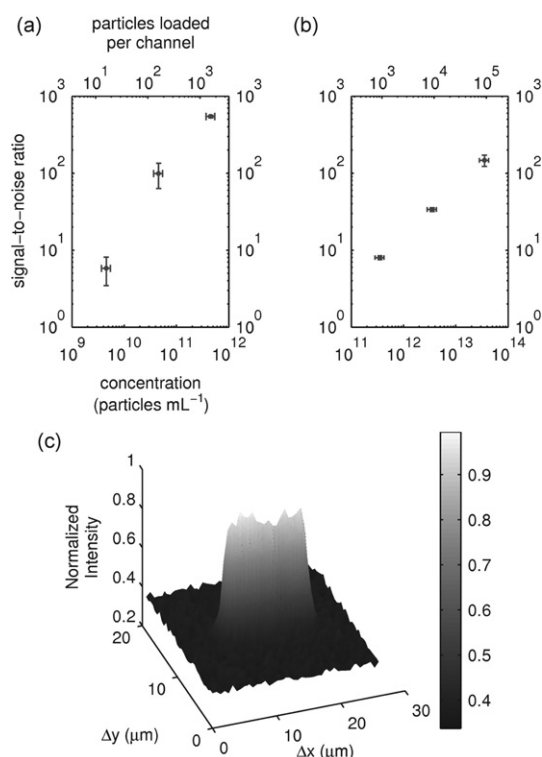


**Fig. 6** SNR of (a) trapped 120-nm particles and (b) trapped 30-nm particles. The SNR plotted against analyte concentration suggests a nearly linear relationship. The horizontal error bars for each point correspond to the calculated number of particles loaded in each channel, as shown by the top  $x$ -axis. In each instance, the SNR data were captured at  $\sim 24$  s following the first detected signal at the interface. (c) Typical contour plot for the fluorescent signal of trapped 120-nm particles at a concentration of  $4.55 \times 10^{10}$  particles  $\text{mL}^{-1}$ .

## 4 Conclusions

Nanofluidic devices offer a new approach with advantages compared to common techniques to analyze nanoparticles. Our implementation employed nanochannel dimensions to separate or trap nanoparticles. We developed a thin film nanofluidic device capable of quickly trapping analytes based on capillary flow. These nanofluidic channels were made with two segments of different heights to physically trap and concentrate analytes in a solution. We trapped nano-scale polymer beads and viral capsids, and measured their fluorescent intensities, which showed excellent SNR at very low concentrations for several nanoparticles. The detection system could be further improved by increasing optical power density instead of using wide-field optics, and by implementing an intensified CCD camera system capable of single photon detection. Our results indicate that such a system could be used for a wide range of nano-scale size-based separations.

Size trapping in a nanofluidic device could be helpful to isolate and observe bio-macromolecular complexes. These complexes are made up of multiple proteins, nucleic acids, and other biological macromolecules (*e.g.* viruses, ribosomes, and enzyme complexes). Trapping these complexes in a nanofluidic device would (1) provide a chamber to perform “small-scale” experiments, (2) give additional ability to isolate complexes that remain “impure” despite multiple centrifugation, precipitation, or chromatographic separation steps, and (3) allow concentration and observation of very small amounts of sample. Many macromolecular complexes are extremely dilute or exist only in very small amounts. A scarce complex of a certain size might co-elute in a chromatography column or equilibrate at the same density (in centrifugation) as a plentiful complex of a different size. A nanofluidic device could be used to extract that scarce complex from the mixture.

Other size-specific trapping applications and designs could be developed beyond what is reported here. For example, a two-segment device could be used to separate a binary mixture of analytes, where one analyte becomes trapped at the interface and the smaller analyte travels the full length of the channel. Another implementation would utilize size-specific trapping devices consisting of more than two segments, allowing for separating and trapping a greater number of analytes. Another application includes concentrating nano-scale analytes into a small volume where they could be studied using optical methods similar to those used with cuvettes. Selective trapping is an effective method of isolating and concentrating nanoparticles, and it can be further extended to become a powerful separation mechanism for nanofluidics.

## 5 Acknowledgements

We would like to thank William Newcomb and Jay Brown (University of Virginia) for providing the HSV-1 sample and Zachary Porterfield and Adam Zlotnick (Indiana University) for providing the HBV capsids.

## References

- 1 J. C. T. Eijkel and A. van den Berg, *Microfluid. Nanofluid.*, 2005, **1**, 249–267.
- 2 M. Baba, T. Sano, N. Iguchi, K. Iida, T. Sakamoto and H. Kawaura, *Appl. Phys. Lett.*, 2003, **83**, 1468–1470.
- 3 P. Abgrall and N. T. Nguyen, *Anal. Chem.*, 2008, **80**, 2326–2341.
- 4 T. Ito and S. Okazaki, *Nature*, 2000, **406**, 1027–1031.
- 5 P. Rai-Choudhury, *Handbook of Microlithography, Micromachining and Microfabrication*, IET, 1997, pp. 131–232.
- 6 P. Mao and J. Han, *Lab Chip*, 2005, **5**, 837–844.
- 7 J. Fu, J. Yoo and J. Han, *Phys. Rev. Lett.*, 2006, **97**, 018103.
- 8 N. Kaji, Y. Tezuka, Y. Takamura, M. Ueda, T. Nishimoto, H. Nakanishi, Y. Horiike and Y. Baba, *Anal. Chem.*, 2004, **76**, 15–22.
- 9 C.-H. Chen and J. G. Santiago, *J. Microelectromech. Syst.*, 2002, **11**, 672–683.
- 10 B. A. Peeni, M. L. Lee, A. R. Hawkins and A. T. Woolley, *Electrophoresis*, 2006, **27**, 4888–4895.
- 11 M. B. Stern, M. W. Geis and J. E. Curtin, *J. Vac. Sci. Technol., B*, 1997, **15**, 2887–2891.
- 12 S. W. Turner, A. M. Perez, A. Lopez and H. G. Craighead, *J. Vac. Sci. Technol., B*, 1998, **16**, 3835–3840.
- 13 M. Foquet, J. Korch, W. Zipfel, W. W. Webb and H. G. Craighead, *Anal. Chem.*, 2002, **74**, 1415–1422.
- 14 N. R. Tas, J. W. Berenschot, P. Mela, H. V. Jansen, M. Elwenspoek and A. van den Berg, *Nano Lett.*, 2002, **2**, 1031–1032.
- 15 P. Mela, N. R. Tas, E. J. W. Berenschot, J. van Nieuwkastele and A. van den Berg, *Electrophoresis*, 2004, **25**, 3687–3693.
- 16 B. A. Peeni, D. B. Conkey, J. P. Barber, R. T. Kelly, M. L. Lee, A. T. Woolley and A. R. Hawkins, *Lab Chip*, 2005, **5**, 501–505.
- 17 J. P. Barber, E. J. Lunt, Z. A. George, D. Yin, H. Schmidt and A. R. Hawkins, *IEEE Photonics Technol. Lett.*, 2006, **18**, 28–30.
- 18 M. N. Hamblin, J. M. Edwards IV, M. L. Lee, A. T. Woolley and A. R. Hawkins, *Biomicrofluidics*, 2007, **1**, 034101.
- 19 J. M. Edwards IV, M. N. Hamblin, H. V. Fuentes, B. A. Peeni, M. L. Lee, A. T. Woolley and A. R. Hawkins, *Biomicrofluidics*, 2007, **1**, 014101.
- 20 H. A. Reed, C. E. White, V. Rao, S. A. B. Allen, C. L. Henderson and P. A. Kohl, *J. Micromech. Microeng.*, 2001, **11**, 733–737.
- 21 W. Li, J. O. Tegenfeldt, L. Chen, R. H. Austin, S. Y. Chou, P. A. Kohl, J. Krotine and J. C. Sturm, *Nanotechnology*, 2003, **14**, 578–583.
- 22 J. P. Barber, D. B. Conkey, J. R. Lee, N. B. Hubbard, L. L. Howell, D. Yin, H. Schmidt and A. R. Hawkins, *IEEE Photonics Technol. Lett.*, 2005, **17**, 363–365.
- 23 N. B. Hubbard, L. L. Howell, J. P. Barber, D. B. Conkey, A. R. Hawkins and H. Schmidt, *J. Micromech. Microeng.*, 2005, **15**, 720–727.
- 24 K. R. Williams, K. Gupta and M. Wasilik, *J. Microelectromech. Syst.*, 2003, **12**, 761–778.
- 25 J. Fu, P. Mao and J. Han, *Trends Biotechnol.*, 2008, **26**, 311–320.
- 26 L. A. Woods, T. P. Roddy, T. L. Paxon and A. G. Ewing, *Anal. Chem.*, 2001, **73**, 3687–3690.
- 27 S. Pennathur and J. G. Santiago, *Anal. Chem.*, 2005, **77**, 6772–6781.
- 28 S. Pennathur and J. G. Santiago, *Anal. Chem.*, 2005, **77**, 6782–6789.
- 29 C. C. Striemer, T. R. Gaborski, J. L. McGrath and P. M. Fauchet, *Nature*, 2007, **445**, 749–753.
- 30 H. D. Tong, H. V. Jansen, V. J. Gadgil, C. G. Bostan, E. Berenschot, C. J. M. van Rijn and M. Elwenspoek, *Nano Lett.*, 2004, **4**, 283–287.
- 31 C. J. M. van Rijn, G. J. Veldhuis and S. Kuiper, *Nanotechnology*, 1998, **9**, 343–345.
- 32 J. Han and H. G. Craighead, *J. Vac. Sci. Technol., A*, 1999, **17**, 2142–2147.
- 33 E. W. Washburn, *Phys. Rev.*, 1921, **17**, 273–283.
- 34 N. R. Tas, J. Haneveld, H. V. Jansen, M. Elwenspoek and A. van den Berg, *Appl. Phys. Lett.*, 2004, **85**, 3274–3276.
- 35 A. Han, G. Mondin, N. G. Hegelbach, N. F. de Rooij and U. Staufer, *J. Colloid Interface Sci.*, 2006, **293**, 151–157.
- 36 J. Haneveld, N. R. Tas, N. Brunets, H. V. Jansen and M. Elwenspoek, *J. Appl. Phys.*, 2008, **104**, 014309.
- 37 N. Goedecke, J. Eijkel and A. Manz, *Lab Chip*, 2002, **2**, 219–223.
- 38 M. Zimmermann, S. Bentley, H. Schmid, P. Hunziker and E. Delamarche, *Lab Chip*, 2005, **5**, 1355–1359.
- 39 M. Wang, M. Benford, N. Jing, G. Coté and J. Kameoka, *Microfluid. Nanofluid.*, 2009, **6**, 411–417.
- 40 M. Wang, N. Jing, I.-H. Chou, G. L. Cote and J. Kameoka, *Lab Chip*, 2007, **7**, 630–632.
- 41 P. G. Arduino and S. R. Porter, *J. Oral Pathol. Med.*, 2008, **37**, 107–121.
- 42 R. Patient, C. Hourieux, P.-Y. Sizaret, S. Trassard, C. Sureau and P. Roingeard, *J. Virol.*, 2007, **81**, 3842–3851.
- 43 K. G. H. Janssen, H. T. Hoang, J. Floris, J. de Vries, N. R. Tas, J. C. T. Eijkel and T. Hankemeier, *Anal. Chem.*, 2008, **80**, 8095–8101.